Photonic band gaps in highly conformal inverse-opal based photonic crystals

D. Gaillot, T. Yamashita, and C. J. Summers
School of Materials Science and Engineering, Georgia Institute of Technology, Atlanta, Georgia 30332-0245, USA
(Received 4 May 2005; revised manuscript received 18 July 2005; published 7 November 2005)

Large three-dimensional photonic band gap (PBG) structures offer revolutionary advances in controlling light emission and propagation. However, current techniques are not yet adequate to fabricate large area structures with optimum photonic properties. Inverse shell opals offer a "bottom-up" approach to fabrication but are limited by the small full PBG and the lack of appropriate materials for operation in the visible where most impact is expected. From photonic band and electric-field power profile investigations in inverse shell opals, we describe the effect of the dielectric backbone geometry on gap size and minimum refractive index contrast to sustain a full PBG. The results enable us to identify the mechanisms limiting the PBG and to show that feasible photonic crystals based devices using low index materials could result in larger full PBGs in the visible.

DOI: 10.1103/PhysRevB.72.205109 PACS number(s): 42.70.Qs, 41.20.Jb, 78.66.Sq

I. INTRODUCTION

In the late 1980s a class of photonic structures, called photonic crystals (PCs), emerged under the innovation of Yablonovitch and John.[1,2] They proposed that, under specific conditions, photonic band gaps (PBGs) or stop bands, spontaneous emission rate modifications, and strong Anderson localization would occur in periodically modulated dielectric materials. A PC consists of a material with a periodically modulated refractive index in one, two, or three dimensions, which strongly affects the photonic density of states (DOS). In certain cases, the DOS goes to zero for a range of photon energies known as the PBG. Photons within a PBG (with a wavelength that approximately matches that of the dielectric period) are not allowed to either propagate through, or to be emitted from the crystal. However, allowed modes can be engineered within the forbidden DOS region by introducing donor or acceptor defects.[3] Control of these fundamental properties potentially offers a tremendous enhancement over conventional photonic devices enabling: low-threshold or thresholdless microemitters, ultrafast optical switches, beam steering, waveguiding, PBG/Holy fibers or even narrow spectrum light emitting diodes (LEDs).[4–10]

II. BACKGROUND

A PCs optical properties are characterized by their photonic band diagrams, which define the allowed photon frequencies (ω_n) to photon wave vector (k) relationships within the crystal. Many simulation techniques, such as three-dimensional (3D) finite-difference-time-domain (FDTD) and plane-wave expansion (PWE), have been developed over the last 15 years to compute these band diagrams and are the essence of any PC investigations. Their predictions have fueled the development of fabrication tools to design nanometer-scale 3D features. Early calculations predicted that 3D PCs with the diamond, diamondlike, or more generally fcc lattices, can create large PBGs for values of refractive index contrast as low as 2.0 for the diamond structure as reported by Ho and coworkers.[11,12] However, many 3D PBG structures cannot be made using traditional "top-down" semiconductor fabrication approaches, thus the introduction of "bottom-up" self-assembly techniques to achieve large-scale fcc structures provided a major fabrication breakthrough.[13] Current techniques support the fabrication of high-quality opals, which enable consistent PBG properties over a large scale.[14] Synthetic opals were first predicted as good candidates to achieve 3D light confinement,[15] but, the low refractive index n of a silica opal ($n \sim 1.4$) only opens directional or pseudo-PBGs (PPBGs) between the second and third bands in the photonic band diagram. However, the air voids, which represent $\sim$26% of the opal volume, can be homogeneously or partially filled in to create an infiltrated opal as shown in Fig. 1(a). Figure 1(b) shows the inverted structure that can be formed by selectively etching the dielectric spheres to leave air spheres within a high dielectric constant material backbone. Theoretically, the latter dielectric/air network topology has been shown theoretically to create an omni-directional or full-PBG (FPBG) between the eighth and ninth photonic bands if the refractive index contrast is sufficiently high (>2.8).

Experimentally, many approaches have been considered to fabricate inverse synthetic opals. Electrochemical, chemical conversion or sol-gel techniques were demonstrated to provide a dielectric total volume fraction from 0% to $\sim$26%. 3D PBG structures with a refractive index contrast >2.8 operating from the near-visible to the microwave range, as expected by homogeneous infiltration models, have been successfully fabricated.[16–18] A second approach was driven by Wijnhoven and Vos who recently reported the fabrication of partially filled inverted opals where a titania backbone was obtained by precipitation from a liquid-phase chemical reaction.[19] Busch and John theoretically investigated the PBG properties of partially filled inverse opals as presented in Fig. 1(c), using a PWE simulation coupled with an overlapping sphere model.[20,21] These structures are commonly referred to as inverse shell opals or highly conformal inverse opals in which the coating conforms to the topography of the spheres and consequently leaves air pockets at the interstitials. Figure 1(d) shows that the interstitials of an inverse

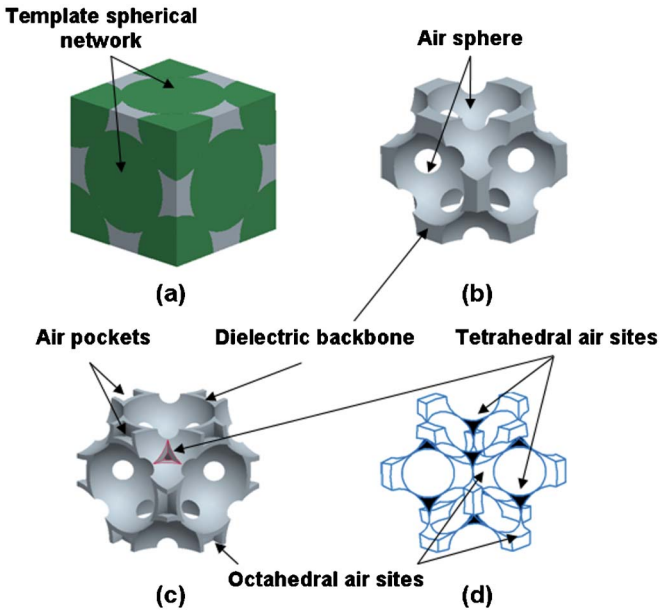

FIG. 1. (Color online) (a) Unit cell of a fully 3D infiltrated opal. (b) Unit cell of a homogeneously filled inverse opal where the spheres have been chemically etched away leaving a dielectric backbone in air. (c) 3D unit cell of an inverse shell opal obtained using a conformal infiltration technique and where the dielectric total volume fraction achieved is 22.4%. (d) 3D view of the air network formed in an inverse opal in which the dielectric total volume fraction is lower than 22.4%. (Dielectric backbone has been graphically removed for clarity; tetrahedral and octahedral air sites connected by thin air channels are, respectively, presented in black and white.)

shell opal form a network composed of air channels connecting octahedral and tetrahedral air sites. The octahedral air sites form a fcc air lattice shifted from the main fcc air lattice by half a unit cell while the tetrahedral air sites form a simple cubic (SC) air lattice with a smaller lattice constant. As infiltration increases and due to the fcc geometry, these air channels eventually close preventing the dielectric material from completely filling the octahedral and tetrahedral interstitial sites. Due to a higher surface area/volume ratio in the octahedral geometry, it has to be noticed that the octahedral air sites are filled much quicker than the tetrahedral sites with increasing infiltration. However, the tetrahedral air sites which have a lower volume compared to that of the octahedral air sites are completely filled before the octahedral air sites. Hence, the interstitial volume can be only conformally coated to ~86% of the air volume by dielectric material (equivalent to 22.4% of the total opal volume fraction) leaving octahedral and tetrahedral air pockets within the dielectric backbone, as shown in Fig. 1(c). Therefore, inverse shell opals with a total volume fraction greater than 22.4% cannot be made using conformal infiltration. To date, a wide range of materials has been reported to be used to infiltrate opal templates from oxides, polymers, metals, glasses, and luminescent materials.[18,19,22–36] Fabrication achievement came from the recent report of complete PBG inverse shell opals operating in the infrared using chemical vapor deposition[37,38] (CVD) to infiltrate silicon or germanium.

However, the gap is typically lower than predicted for the case of full infiltration. For the hypothetical situation for conformal infiltrations exceeding 86%, Busch and John reported that a silicon inverse shell opal exhibits an enhanced gap ($\Delta\omega/\omega_0$) of 8.5% when the infiltration was equivalent to 97.7% of the air interstices (25.4% total volume fraction of silicon). For a 100% conformal infiltration, a gap of 4.5% was predicted.[20] Here, we investigate the gap formation mechanisms in inverse shell opals when the fraction of dielectric material varies from a few percent to 100%. The understanding of these mechanisms could ultimately unveil a practical way to enhance PBG properties for the whole range of infiltration by modifying the dielectric/air network topology of inverse shell opals or related structures. From an experimental point of view, homogeneous infiltration based approaches cannot provide sufficient engineered modifications of the dielectric backbone. Recently, King *et al.* have demonstrated the robustness and flexibility of the atomic layer deposition (ALD) as a bottom-up technique for modifying the shell structure with an unprecedented degree of control and repeatability using a variety of high refractive index materials.[39,40] This approach can be used for designing complex inverse structures in which a full PBG operating in the visible would have a tremendous impact in traditional areas such as the display market (high-definition flat panels, low-consumption highly-efficient LEDs, etc.).

Using 3D-FDTD calculations coupled with electric-field power profile maps, we have investigated the photonic properties of inverse shell opals fabricated using a conformal coating model. The purpose of this study is to identify the mechanisms responsible for the strong influence of the conformal dielectric/air network topology on the inverse opals PBGs properties: photonic gap width and FPBG refractive index contrast requirement. From our findings, we show how analysis of the electric-field power profiles can help to predict experimentally achievable structures that have a full photonic band gap and a reduced refractive index contrast requirement.

III. SIMULATIONS

Many simulations techniques are currently available to evaluate photonic band diagrams and other properties of PCs. Among them, 3D-FDTD is the most versatile and robust tool. To compute a band diagram, allowed modes have to be found for a particular k vector in reciprocal space. In this technique, Maxwell's equations are discretized both in space and time using central derivative approximations. Electric and magnetic fields are shifted following Yee's work to implicitly satisfy Gauss and Ampere's equations.[41] The first irreducible Brillouin zone edges of the fcc crystal shown in the bottom inset in Fig. 2 are also discretized into evenly spaced k vectors. For each k vector, fields which follow Bloch's theorem are initiated at time $t=0$ within the computational cell[42] for an inverse opal and sequentially interact with the complex dielectric nature of the PC. The top-left inset in Fig. 2 presents how an inverse opal is parameterized to compute a normalized dielectric function. A fine mesh of $50\times50\times50$ points per unit cell has been consistently used

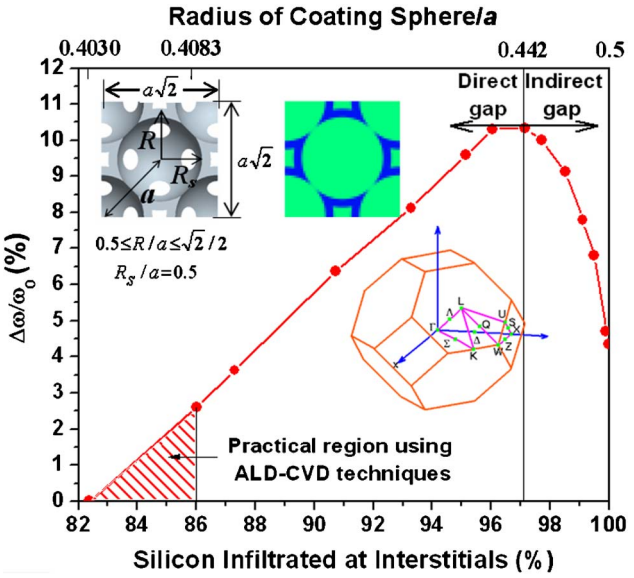

FIG. 2. (Color online) Dependence of the FPBG of inverse opals as a function of the infiltrated percentage of the air voids for a conformally infiltrated silicon. The dashed area indicates the practical region in which these structures can be made by ALD or CVD techniques. Top left inset shows top view parametrization of an inverse shell opal while the right inset shows the computational cell used to calculate the corresponding photonic band diagram. The first Brillouin zone of a fcc crystal is presented in the bottom right inset.

in this work, as shown in the top-right inset in Fig. 2. The complex dielectric function of inverse opals is modeled with good accuracy while preserving computing time. Furthermore, an infinite crystal can be simulated by applying Bloch conditions at the edges of the unit cell. The electromagnetic fields at time $t+\Delta t$ are then updated from the previous fields at time t. After sufficient time steps, the system eventually converges to a solution where only allowed modes exist inside of the PC. Typically, a stable solution has been observed for a number of steps greater than 30 000 which also yields a sufficient spectral resolution. At each time step, the fields are recorded at random points in space. Finally, the code performs a fast Fourier transform (FFT) on these points to calculate the power spectrum. Allowed frequencies are extracted from this spectrum, normalized with respect to the PC geometry ($\omega_n = a/\lambda$, where a is the fcc lattice constant) and finally saved. Then, the code moves on to the next k vector where the same protocol is repeated. The whole simulation stops when all k points are evaluated. The allowed frequencies versus k-vectors are then plotted to form the photonic band diagram.

Electric-field power maps were simulated using a modified version of the 3D-FDTD code designed for band diagrams. A normalized frequency and k vector of interest were chosen from the previously calculated band diagram and are used as input parameters. In this case, modulated Gaussian pulses vibrating at the desired frequency are activated within the computational cell and interact with the PC. Sufficient time is allowed so that the parasite modes are totally dissipated, then the excited electric fields are recorded in the entire computational cell at each time step. A discrete Fourier transform (DFT) is performed as long as the simulation runs and the terms at the final time step correspond to the electric power field profiles. This approach has proven to be very successful and fast to investigate field distributions within 3D PCs.

IV. RESULTS AND DISCUSSION

The photonic band diagrams of partially filled inverse opals with infiltrations ranging from 0% to 100% of the air void volume were calculated for silicon ($n=3.45$). Figure 2 presents the evolution of the PBG as a function of infiltration percentage of the air interstitials from 82% to 100%. The infiltration percentage is related to the backbone thickness which is expressed as the ratio of the radius of the coating sphere R to the cubic lattice constant a, from $R/a=0.4026$ to $R/a=0.5$. Four particular cases can be pointed out from Fig. 2. First, a FPBG is only obtained when the percentage of silicon infiltration reaches 82.37% of the air void volume as shown in Fig. 3(a). In this configuration a strong pseudo PBG is already sustained over the X-Γ-L-U-X space between the eighth and ninth bands, and it is the W point that is responsible for the complete gap that opens between the eighth and ninth bands. Figure 3(b) presents the shell band diagram at the practical conformal fabrication limit for an 86% silicon inverse shell opal in which the eighth and ninth bands at the W point have split, hence, exhibiting a complete gap. Further dielectric infiltration of the air voids volume cannot be achieved since the connected channels become completely filled. At this point the thin air channels have vanished leaving octahedral air pockets within the dielectric backbone. Nevertheless, assuming that is possible to increase the conformal infiltration then a maximum gap is observed at $R/a=0.442$ when the tetrahedral sites are almost fully infiltrated at 97.2% of void volume, corresponding to 25.3% of total volume. Figure 3(c) presents the band diagram of the optimized structure with a 10.34% gap ($\Delta\omega/\omega_0$), in good agreement with Busch and John's calculations.[20,21] The dashed region represents the FPBG where the lower boundary is defined by the eighth band at the W point, and the upper boundary is defined by the ninth band at the W and X points. At 100% of conformal infiltration, the octahedral air sites are totally filled to form a full inverted opal in which a FPBG of 4.34% is calculated as shown in Fig. 3(d). These photonic band diagrams clearly indicate that the PBG properties are intimately linked to the activity of the W and X points at the eighth and ninth bands. Figure 4 shows the frequency dependence of the eighth band which occurs at the W point and the bottom of the ninth band which occurs at the W and X points plotted as a function of the normalized radius of the silicon coating sphere R/a from value of 0.4030 to 0.5. Band diagrams indicate that below $R/a=0.442$, the W-W gap between the eighth and ninth bands directly defines the photonic band gap. It is observed that, as the percentage of dielectric material increases, the eighth band at the W point decreases at a faster rate than the ninth band at the same point, such that the band gap naturally increases. With increasing infiltration, the average refractive index increases

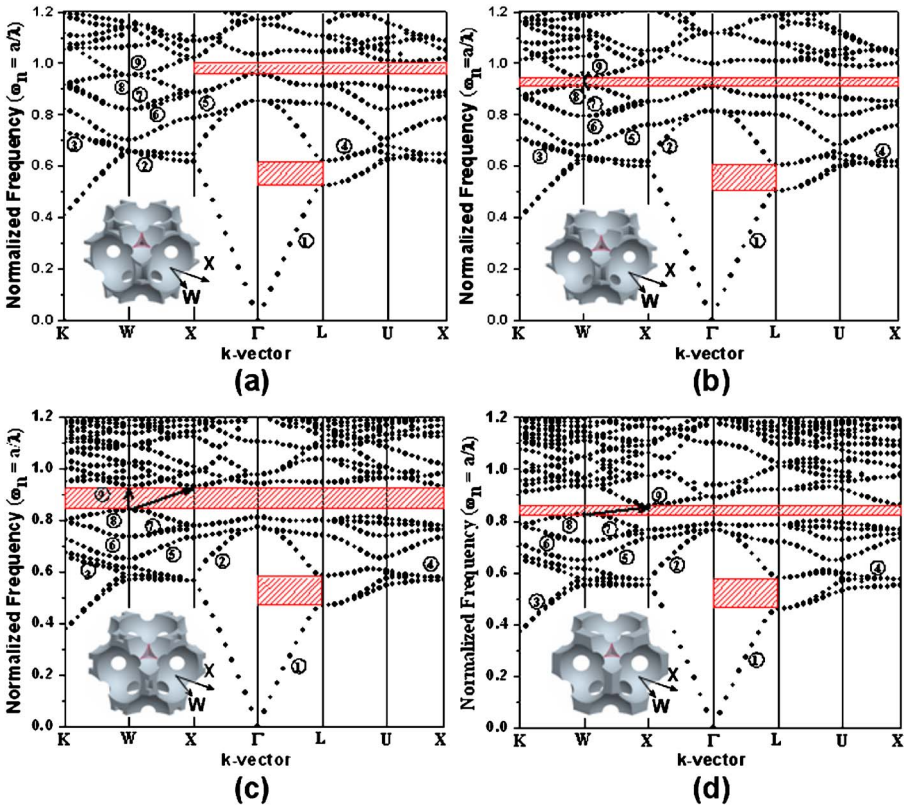

FIG. 3. (Color online) Band diagrams of silicon inverse shell opals as a percentage of air void infiltration. (a) Infiltration of 82.37% (R/a=0.4030). The connection of the eighth and ninth bands at the W point prevents the formation of a complete photonic band gap. (b) 86% inverse shell opal (R/a=0.4083). The arrow shows the direct gap of 2.61% obtained between the eighth and ninth bands of the W point. (c) 97.2% inverse shell opal (R/a=0.442). The arrows show the optimized direct and indirect gaps obtained between the eighth band of the W point and the ninth band of the X and W points. (d) 100% inverse opal (R/a=0.5). Indirect gap is shown by the arrow between the eighth band of the W point and the ninth band of the X point. For each band diagram, the corresponding unit cell is presented at the bottom right.

and the eighth band at the W point shifts down accordingly. Moreover, the X point of an upper band (we reference to an "upper" band whenever this band lies above the ninth band) is initially at a much higher frequency, but decreases in frequency at a higher rate while the ninth band at the W point is less affected. The maximum photonic gap occurs when the X and W point of the ninth band are at the same frequency. The dotted vertical line in Fig. 4 shows the transition between the direct W-W and the indirect W-X photonic band gap which occurs when R/a=0.442. (Band crossing occurs for an exact geometry where the X and W points of the ninth band lie at the same frequency.) An additional increase in R, corresponding to the addition of dielectric material induces these two bands to cross. For higher values of R, the eighth band at the W point and the ninth band at the X point define an indirect photonic band gap.

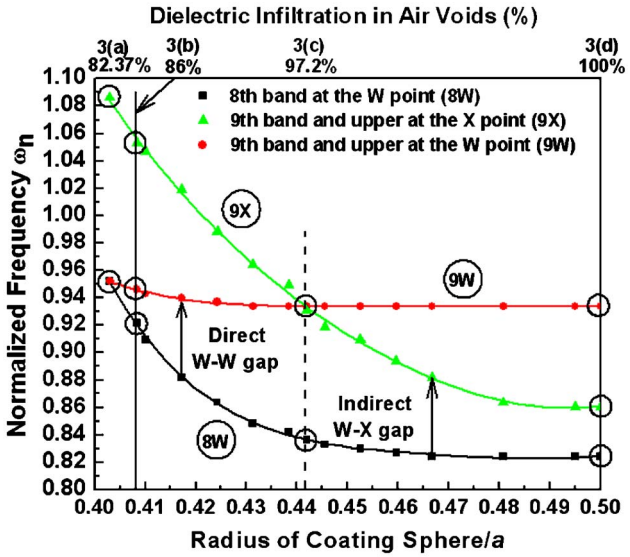

FIG. 4. (Color online) Evolution of the eighth band at the W point and ninth band at the W and X points as a function of silicon infiltration. The degree of infiltration is expressed in terms of the radius of coating sphere R/a where the cubic lattice constant is a. The bold vertical line corresponding to R/a=0.442 shows the transition between the W-W and the W-X gap domination. Band crossing occurs at that exact geometry where the bottom of the X and W bands lie at the same frequency.

As discussed previously, conformal techniques only allow infiltration of dielectric material up to ~86% of the interstitial air void. However, 86% inverse shell opals structures calculated as a function of refractive index show a PBG only when $n>2.8$. Because few materials have $n>2.8$, silicon (n=3.45) for example, this limits operation to the near-IR range since silicon is opaque at higher frequencies. In order to investigate the use of other high refractive index materials, we have studied the behavior of full inverse and inverse shell opals for refractive indices ranging from 2.8 to 4.0 using the same procedure. These results demonstrate that a photonic band gap is obtained for a minimum refractive index contrast of ~3.3 for an 86% inverse shell opal compared to ~3.0 for a full inverse opal and ~2.85 for a 97.2% inverse shell opal where the maximum gap is observed (R/a=0.442), as shown in Fig. 5. This result prevents the use of highly conformal inverse opals in the visible range. Figure 5 also indicates that indirect PBG inverse shell opals have a lower PBG refractive index requirement than inverse shell opals in which a direct gap is observed. Prior to obtaining a direct gap, the eighth

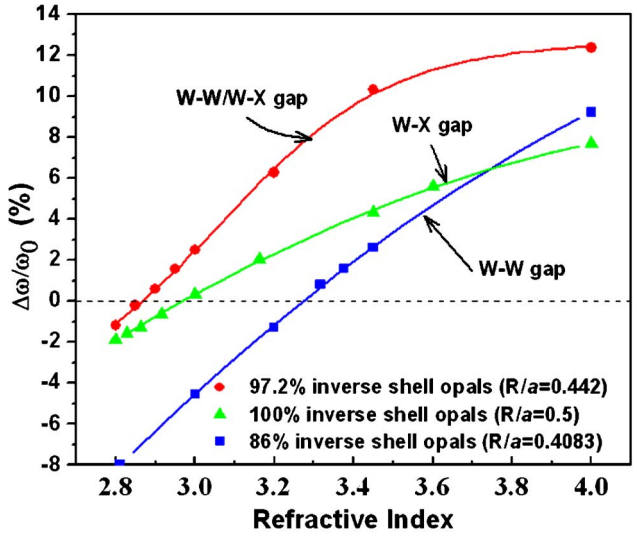

FIG. 5. (Color online) Evolution of the gap/midgap ($\Delta\omega/\omega_0$ in %) as a function of refractive index for an 86%, an optimized 97.2%, and a full infiltrated silicon inverse shell opal.

and ninth bands cross each other at the *W* point defining a "negative" direct gap width. Although this does not present any meaning, the slopes of the curves in the vicinity of the gap formation give us additional band activity information. The inverse shell opal that exhibits a direct/indirect gap provides the lowest PBG refractive index requirement for any

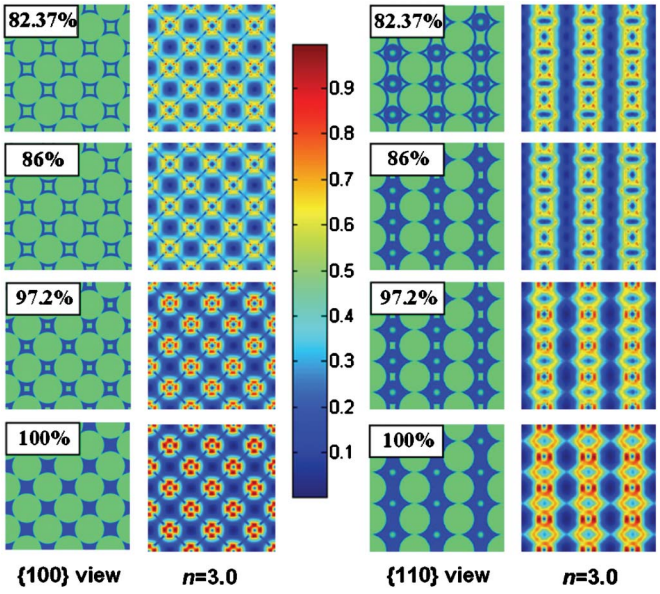

FIG. 6. (Color online) Evolution of electric-field power maps for the eighth band at the *W* point for inverse structures at the infiltration percentage indicated by the circles in Fig. 4 and a refractive index value of 3.0. The first and third columns respectively depict the physical dielectric structure in {100} and {110} planes of the unit cell while the second, and fourth columns show the corresponding field profiles. Field profiles from the top row to the bottom row, respectively, correspond to an inverse shell opal in which 82.37%, 86%, 97.2%, and 100% of the interstitial air volume has been infiltrated with dielectric material.

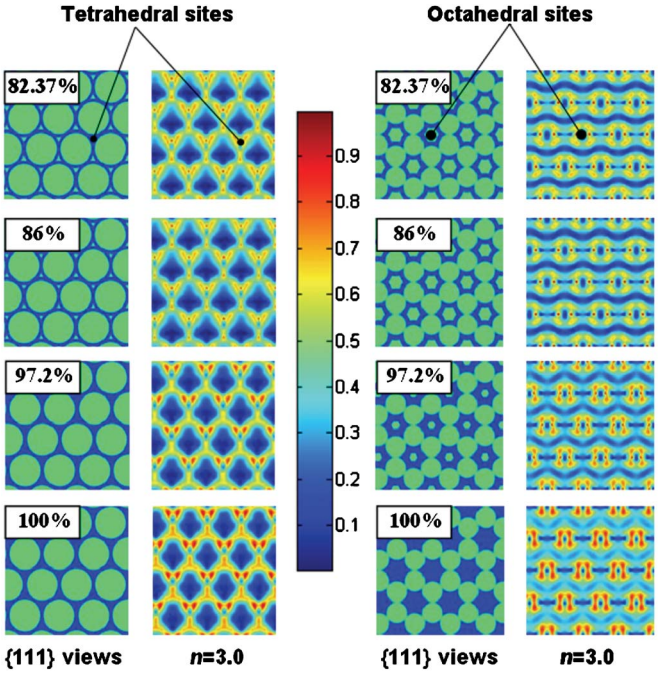

FIG. 7. (Color online) Evolution of electric-field power maps for the eighth band at the *W* point for inverse structures at the infiltration percentage indicated by the circles in Fig. 4 and refractive indices varying from 2.8 to 3.45. The first two columns, respectively, depict the physical dielectric structure at offset {111} planes of the unit cell highlighting the tetrahedral and octahedral sites, while the second, and fourth pair of columns show the corresponding field profiles. Field profiles from the top row to the bottom row, respectively, correspond to an inverse shell opal in which 82.37%, 86%, 97.2%, and 100% of the interstitial air volume has been infiltrated with dielectric material.

scenario. It has to be noticed as well that in the low refractive index region, the slopes of the direct PBG structures (from 86% to 97.2% of conformal infiltration in the interstitials air sites) are similar and that the slope for indirect PBG structures (from 97.2% to 100% of conformal infiltration in the interstitials air sites) is lower. On the other hand, for refractive indices greater than ~3.4, the slopes of indirect PBG structures are similar and the slope of the direct PBG structure is higher. From Fig. 5, we can conclude that direct gap structures are much more dependent on the refractive index contrast than are indirect gap structures. Thus, a structure that would exhibit a wide indirect gap is more likely to have a lower refractive index requirement contrast than structures in which a direct gap at the same width is observed.

It follows from this discussion that the topology of the dielectric/air network in shell opals plays a key-role by enhancing the band gap as reported previously,[20,21] but its drastic effect on the FPBG opening condition in an inverse shell opal has not been studied to date. Thus, to more precisely study the effect of the air network on the FPBG, 3D-FDTD electric-field power profiles of the gap boundaries at the *W* and *X* point were investigated as a function of infiltration for refractive indices varying from 2.8 to 3.45. The electric field power distribution was computed in the 3D unit cell for a

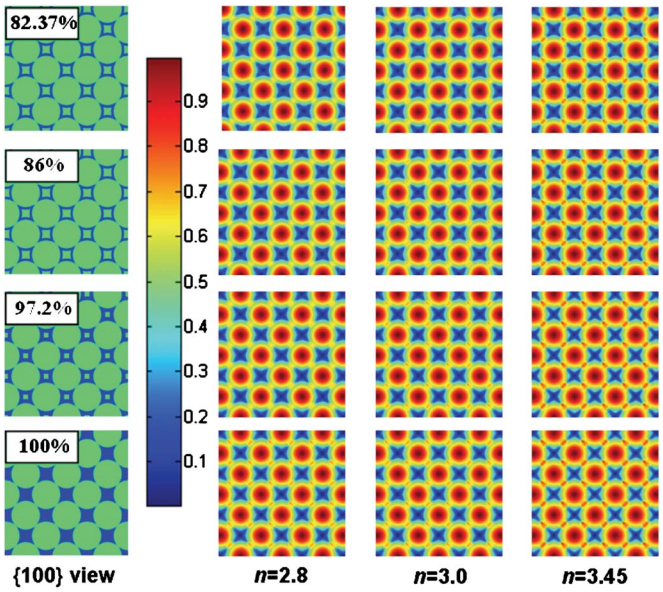

FIG. 8. (Color online) Evolution of electric-field power maps for the upper and ninth band at the *W* point for inverse structures at the infiltration percentage indicated by the circles in Fig. 4 and refractive indices varying from 2.8 to 3.45. The first column, respectively, depict the physical dielectric structure in {100} planes of the unit cell while the second, third, and fourth columns show the corresponding field profiles. Field profiles from the top row to the bottom row, respectively, correspond to an inverse shell opal in which 82.37%, 86%, 97.2%, and 100% of the interstitial air volume has been infiltrated with dielectric material.

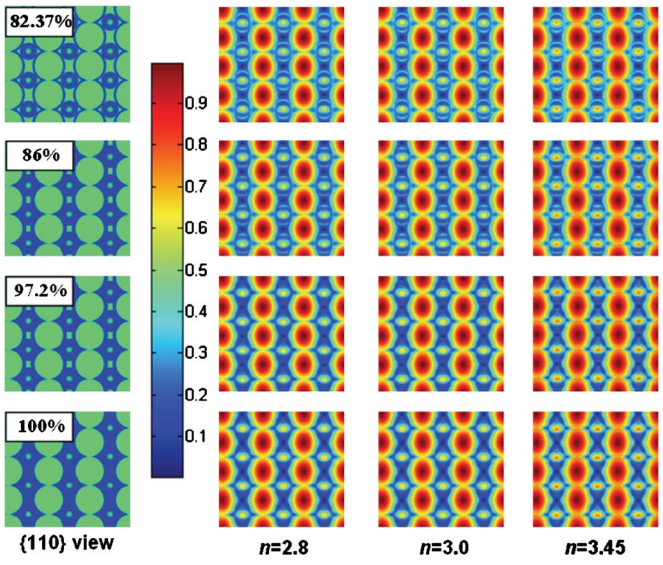

FIG. 9. (Color online) Evolution of electric-field power maps for the upper and ninth band at the *W* point for inverse structures at the infiltration percentage indicated by the circles in Fig. 4 and refractive indices varying from 2.8 to 3.45. The first column, respectively, depicts the physical dielectric structure in {110} planes of the unit cell while the second, third, and fourth columns show the corresponding field profiles. Field profiles from the top row to the bottom row, respectively, correspond to an inverse shell opal in which 82.37%, 86%, 97.2%, and 100% of the interstitial air volume has been infiltrated with dielectric material.

sphere coating thickness ranging from $R/a=0.4030$ to $R/a=0.5$. Additionally, {100}, {110}, and {111} planes of interest have been investigated to simplify the analysis and present the electric power distribution within the tetrahedral and octahedral sites of an inverse shell opal. It has to be noticed that for the case in which a FPBG is not formed ($R/a<0.4030$ for silicon, Fig. 4) the eighth and ninth bands at the *W* point cross and their respective field profiles are switched. In order to be consistent with our analysis, we have assigned the dielectric band to the eighth band and the air band to the ninth band. Due to the numerous results and for clarity, only relevant field profiles are presented.

For the eighth band at the *W* point (bottom of the PBG), Figs. 6 and 7 indicate that the electric-field power increases in the dielectric backbone as the amount of infiltrated material increases from 82.37% to 86%, to 97.2%, and finally 100%. A gradual increase of electric-field power density is expected over this range which explains the discontinuity of the electric-field power density within the backbone between the 86% and 97.2% field profiles due to the large difference of infiltrated material. However, only a refractive index value of 3.0 is presented in Figs. 6 and 7 because an increase of refractive index from 2.8 to 3.45 does not modify the electric-field power density distributions within the backbone, but to a slight degree the power is more concentrated around the dielectric backbone. Thus, as shown previously in Fig. 4, with increasing infiltration the average refractive index increases and the eighth band at the *W* point shifts down accordingly. However, the {111} field profiles from Fig. 7 demonstrate that the presence of octahedral and tetrahedral air sites prevents the electric field from being highly concentrated within these regions of the dielectric backbone. The electric-field power only increases within the dielectric backbone once the volume of air within the tetrahedral sites tends to zero. By the same argument the electric-field power density reaches a maximum value within the backbone as soon as the octahedral air sites totally vanish.

Figures 8–10 show that for the ninth band at the *W* point the field patterns do not change much with increasing thickness of the infiltrated dielectric material although the electric-field power density slightly decreases within the backbone. For all cases, the electric-field power stays in the spherical air domains, and does not concentrate within the remaining tetrahedral and octahedral air sites. These results are very consistent with Fig. 4, which indicates that the frequency activity of the ninth band at the *W* point is not very dependent on increasing infiltration and therefore the introduction of SC and fcc air lattices. However, the {100} and {111} set of field profiles from Figs. 8 and 10, respectively, highlighting the octahedral sites fcc air lattice, also indicate that the electric-field power density located at the sphere overlapping regions increases as the refractive index increases favoring the ninth band at the *W* point to stay at a high frequency as infiltration increases. It follows as well that by increasing the sphere overlapping regions, a higher electric-field power density could be sustained.

The {100}, {110}, and {111} set of field profiles shown in Figs. 11–13 indicate for the ninth band at the *X* point that the electric-field power is concentrated principally in the spheri-

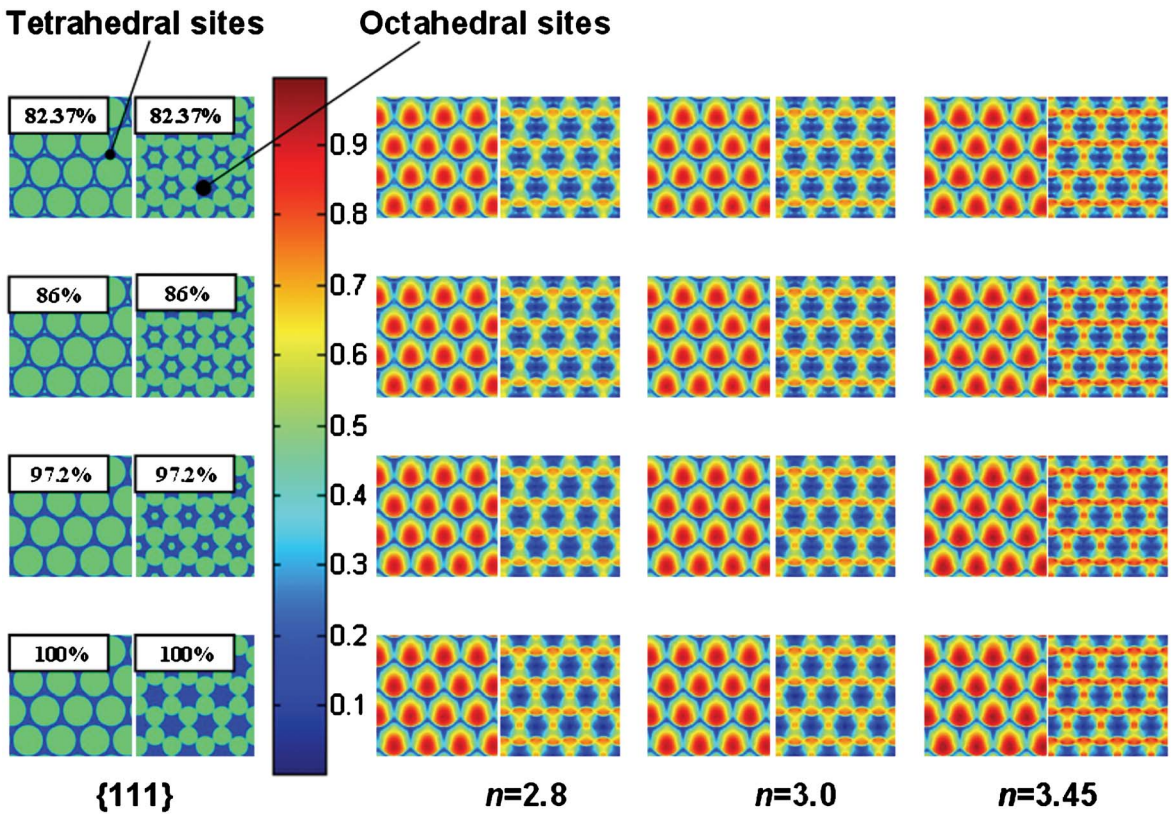

FIG. 10. (Color online) Evolution of electric-field power maps for the ninth band at the *W* point for inverse structures at the infiltration percentage indicated by the circles in Fig. 4 and refractive indices varying from 2.8 to 3.45. The first two columns, respectively, depict the physical dielectric structure at offset {111} planes of the unit cell highlighting the tetrahedral and octahedral sites, while the second, and fourth pair of columns show the corresponding field profiles. Field profiles from the top row to the bottom row, respectively, correspond to an inverse shell opal in which 82.37%, 86%, 97.2%, and 100% of the interstitial air volume has been infiltrated with dielectric material.

cal air domains, octahedral and tetrahedral air sites, but that its density quickly diminishes as the infiltration increases. A detailed look at the evolution of the ninth band at the *X* point in the photonic band diagrams reveals that, as this band shifts down in frequency it eventually crosses other stable bands and it is more likely that the 3D-FDTD simulation picks up a close neighbor air mode increasing the electric-field power density within the spherical air domains of the ninth band mode. These degenerate modes are seen for the 82.37% infiltrated structure at all refractive indices, the 86% case at $n=2.8$ and the 97.2% case at $n=2.8$ and $n=3.0$. As shown previously for the eighth band at the *W* point, the tetrahedral air sites eventually vanish, destroying the connectivity between the octahedral and tetrahedral sites and it is observed that only then is power transferred from the spherical air domains towards the backbone tetrahedral sites. The same phenomenon occurs for the octahedral sites, which disappear at full infiltration thus reinforcing the electric-field power that can be sustained within the octahedral sites of the backbone. As previously observed in Fig. 4, electric-field distributions for the ninth band at the *X* point demonstrate that this band gradually turns from an air band into a dielectric band as infiltration increases. Indeed, as the backbone thickness grows, the dielectric/air periodicity of the structure with respect to the *X* direction is affected considerably by the vanishing of the tetrahedral and octahedral air sites (SC and fcc air lattices) within the backbone. Figure 4 also indicates that the slopes for the *X* point at the upper band and the *W* point at the eighth band are very similar as infiltration increases, but as that structure approaches the optimized geometry (97.2% infiltration), the frequency of the upper band at the *X* point is suddenly pulled down as it crosses the ninth band at the *W* point. This is because the octahedral air sites can no longer sustain a high electric-field power density and any slight increase of infiltrated material promotes a large increase in the electric-field power density within the backbone, which pushes the *X* point frequency down at a higher rate; therefore reducing the indirect gap. As shown previously for the ninth band at the *W* point, these field profiles indicate that electric-field power remains strongly concentrated between neighboring air spheres.

In silicon inverse shell opals, the band gap is formed whenever a certain quantity of dielectric material (dielectric total volume fraction of ~21.4%) is present within the unit cell. The average dielectric constant increases monotonically so one would expect that the direct gap would likewise increase. Electric-field profiles indicate that the *W* point of the eighth band is directly dependent on increasing shell thickness upon infiltration while the *W* point at the ninth band is more dependent on increasing the refractive index. Consequently, the direct gap widens as the average refractive index increases with infiltration, or if the infiltrated material has a

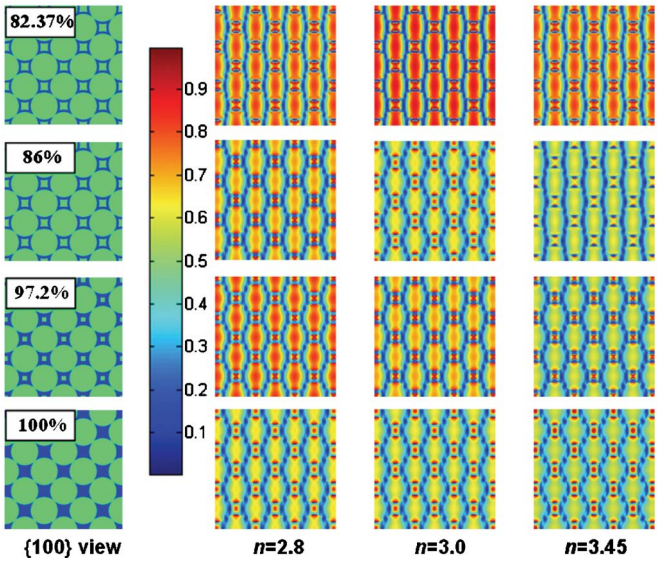

FIG. 11. (Color online) Evolution of electric-field power maps for the upper and ninth band at the *X* point for inverse structures at the infiltration percentage indicated by the circles in Fig. 4 and refractive indices varying from 2.8 to 3.45. The first column, respectively, depicts the physical dielectric structure in {100} planes of the unit cell while the second, third, and fourth columns show the corresponding field profiles. Field profiles from the top row to the bottom row, respectively, correspond to an inverse shell opal in which 82.37%, 86%, 97.2%, and 100% of the interstitial air volume has been infiltrated with dielectric material.

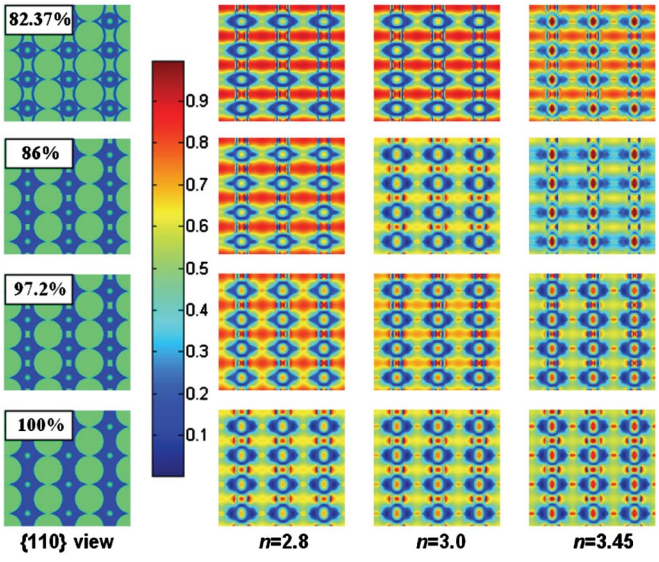

FIG. 12. (Color online) Evolution of electric-field power maps for the upper and ninth band at the *X* point for inverse structures at infiltration indicated by the circles in Fig. 4 and refractive indices varying from 2.8 to 3.45. The first column, respectively, depicts the physical dielectric structure in {110} planes of the unit cell while the second, third, and fourth columns show the corresponding field profiles. Field profiles from the top row to the bottom row, respectively, correspond to an inverse shell opal in which 82.37%, 86%, 97.2%, and 100% of the interstitial air volume has been infiltrated with dielectric material.

higher refractive index. Additionally, it follows that a wider direct gap would be achieved by thickening the dielectric backbone from its inner side. Electric-field profiles for the *X* point at the ninth band quickly evolve upon infiltration, which modifies the power density within the tetrahedral and octahedral air sites. These trapped air pockets are shown to prevent the electric-field power from being concentrated within the dielectric backbone. Furthermore, the air sphere overlapping regions are the preferred locations to sustain high electric-field power whenever the refractive index or the infiltration percentage is low. This behavior relates well to Busch and John's results who reported that the gap width would be enhanced by widening the connection tube diameter.[20,21] The cylinderlike overlapping regions favor the connectivity between the spherical air domains, hence, distributing more efficiently the electric-field power within in the case of an air band. By designing a structure where the electric power is efficiently contained within all the discussed air domains, one could restrict the diffusion of the electric power into the backbone. The *X* band would then be pushed up which would enhance the direct/indirect gap width.

It follows that the direct gap region is dominated by the change in the filling fraction, which pushes the *W* point of the eighth bands down, and the refractive index, which contains the *W* point of the ninth band, from shifting down at the same rate, while the indirect gap region is dominated by the change in the air network topology. There is a competition between these two mechanisms for increasing the direct gap and reducing the indirect gap, despite the fact that they are both closely related to the dielectric/air network topology. Indeed, a maximum gap is observed whenever these two mechanisms balance each other. For a high refractive index, the filling fraction and the shell symmetry are responsible for the direct gap increasing by affecting the activity of the eighth band at the *W* point; nevertheless, the geometry of the octahedral and tetrahedral air network is responsible for reducing the indirect gap by rapidly transforming the ninth band at the *X* point from an air band into a dielectric band. The octahedral and tetrahedral dielectric sites introduced in inverse shell opals are shown to efficiently hold electric power, which becomes important for low refractive index materials where diffusion into the dielectric backbone occurs. Therefore, the air topology affects both the indirect band gap and electric-field power diffusion to the dielectric backbone. It was also shown previously that the refractive index contrast requirement is more likely to decrease significantly if this gap is relatively wide with respect, for instance, to a high refractive index material. On the other hand, direct gap structures were shown to exhibit both a lower gap width and refractive index requirement. It follows that the direct gap can be theoretically optimized, by first designing indirect gap structures presenting a high filling fraction dielectric backbone with no air pockets and larger tubelike air connection between the spherical air domains. From inverse opals, another way to increase the filling fraction is to conformally coat the interior of the dielectric backbone with the same material as demonstrated by Míguez *et al.*[43] Doosje *et al.* have very recently reported that similar fully infiltrated structures theoretically exhibit greater indirect PBG properties.[44]

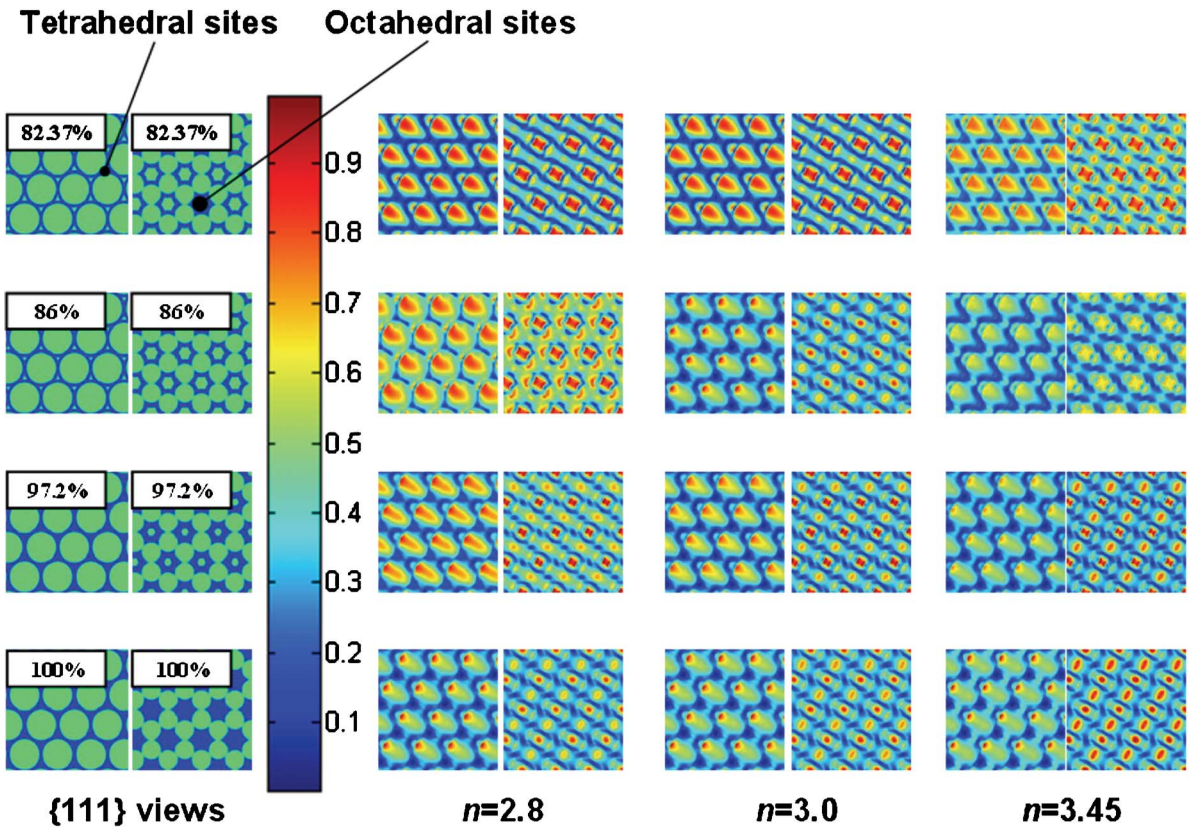

FIG. 13. (Color online) Evolution of electric-field power maps for the upper and ninth band at the X point for inverse structures at the infiltration percentage indicated by the circles in Fig. 4 and refractive indices varying from 2.8 to 3.45. The first two columns, respectively, depict the physical dielectric structure at offset {111} planes of the unit cell highlighting the tetrahedral and octahedral sites, while the second, third, and fourth pair of columns show the corresponding field profiles. Field profiles from the top row to the bottom row, respectively, correspond to an inverse shell opal in which 82.37%, 86%, 97.2%, and 100% of the interstitial air volume has been infiltrated with dielectric material.

Then, geometrically controllable air pockets could be introduced within the dielectric backbone such as in the inverse shell opals to shift the gap from indirect to direct while enhancing the direct FPBG and reducing the refractive index contrast requirement. Therefore, modifications of the current infiltration process using CVD/ALD techniques would potentially yield enhanced direct PBG properties.

V. CONCLUSIONS

In conclusion, we report that an 86% inverse shell opal is predicted to have a minimum refractive index contrast required to opening a FPBG of 3.3 compared to 3.0 for a full inverse opal or even 2.0 in the diamond lattice.[12] Highly conformal inverse opals are intrinsically limited by their geometry and cannot lead to the fabrication of a FPBG material without high refractive index contrast, which restricts their use in the visible because high refractive index materials (with $n>3.3$) transparent in the visible range are not available. Although not experimentally practical, the FPBG width is enhanced in the optimized inverse shell opal, and the refractive index contrast requirement is actually decreased from 3.0 to 2.85. A 10.34% gap has been demonstrated in an optimized silicon inverse shell opal where the air void is 97.2% filled with dielectric material ($R/a=0.442$). Electric-field power profile maps of 3D inverse shell opals are presented and clearly demonstrate the importance of the octahedral and tetrahedral air sites within the backbone and the physics on how they affect the ninth photonic band gap at the X point and the refractive index contrast requirement. The dielectric/air network topology, which is related to the filling fraction, is therefore the cornerstone in controlling both mechanisms: direct/indirect gap size and minimum refractive index contrast. Although the results discussed in this work shows the experimental difficulty of obtaining inverse shell opals with a FPBG in the visible, we discuss how analysis of the electric-field power profiles can help to predict experimentally achievable structures that have a FPBG and a reduced refractive index contrast requirement. Mechanisms that relate the dielectric/air network to the bands behavior, gap size, and FPBG refractive index contrast requirement were then introduced. Finally from our findings, we are currently examining a practical route to enhance PBG properties by investigating PC structures that can be designed using the ALD technique, for example. Indeed, devices working in

such a wide range would be feasible to engineer and manufacture by designing structures that possess these two main characteristics: a high filling fraction to widen the *W*-*W* gap and an air network optimized to prevent the ninth band at the *X* point from limiting the direct gap at low infiltration percentages.

ACKNOWLEDGMENTS

This work was supported by the U.S. Army Research Office under MURI Contract No. DAAD19-01-1-0606. We thank E. Graugnard, J. King, and C. Neff for their many fruitful interactions and discussions.

[1] E. Yablonovitch, Phys. Rev. Lett. **58**, 2059 (1987).
[2] S. John, Phys. Rev. Lett. **58**, 2486 (1987).
[3] R. Meade, K. D. Brommer, A. M. Rappe, and J. D. Joannopoulos, Phys. Rev. B **44**, R13772 (1991).
[4] J. D. Joannopoulos, P. R. Villeneuve, and S. Fan, Nature (London) **386**, 143 (1997).
[5] J. P. Dowling and C. M. Bowden, J. Mod. Opt. **41**, 345 (1994).
[6] S. -Y. Lin, V. Hietala, L. Wang, and E. D. Jones, Opt. Lett. **21**, 1771 (1996).
[7] H. Kosaka, T. Kawashima, A. Tomita, M. Notomi, T. Tamamura, T. Sato, and S. Kawakami, Phys. Rev. B **58**, R10096 (1998).
[8] D. Scrymgeour, N. Malkova, S. Kim, and V. Gopalan, Appl. Phys. Lett. **82**, 3176 (2003).
[9] M. Boroditsky, R. Vrijen, T. F. Krauss, R. Coccioli, R. Bhat, and E. Yablonovitch, J. Lightwave Technol. **17**, 2096 (1999).
[10] S. E. Barkou, J. Broeng, and A. Bjarklev, Opt. Lett. **24**, 46 (1999).
[11] C. T. Chan, S. Datta, K. M. Ho, and C. M. Soukoulis, Phys. Rev. B **50**, R1988 (1994).
[12] K. M. Ho, C. T. Chan, and C. M. Soukoulis, Phys. Rev. Lett. **65**, 3152 (1990).
[13] P. N. Pusey, *Liquids, Freezing and Glass Transition* (Elsevier, New York, 1990).
[14] A. A. Chabanov, Y. Jun, and D. J. Norris, Appl. Phys. Lett. **84**, 3573 (2004).
[15] W. L. Vos, M. Megens, C. M. van Kats, and P. Bosecke, J. Phys.: Condens. Matter **8**, 9503 (1996).
[16] P. V. Braun, R. W. Zehner, C. A. White, M. K. Weldon, C. Kloc, S. S. Patel, and P. Wiltzius, Adv. Mater. (Weinheim, Ger.) **13**, 721 (2001).
[17] B. T. Holland, C. F. Blanford, and A. Stein, Science **281**, 538 (1998).
[18] I. Soten, H. Míguez, S. M. Yang, S. Petrov, N. Coombs, N. Tétreault, N. Matsuura, H. E. Ruda, and G. A. Ozin, Adv. Funct. Mater. **12**, 71 (2002).
[19] J. E. G. J. Wijnhoven and W. L. Vos, Science **281**, 802 (1998).
[20] K. Busch and S. John, Phys. Rev. E **58**, 3896 (1998).
[21] S. John and K. Busch, J. Lightwave Technol. **17**, 1931 (1999).
[22] M. Müller, R. Zentel, T. Maka, S. G. Romanov, and C. M. S. Torres, Adv. Mater. (Weinheim, Ger.) **12**, 1499 (2000).
[23] A. Xiang, J. P. Gao, H. K. Chen, J. G. Yu, and R. M. Liu, Chin. Chem. Lett. **15**, 228 (2004).
[24] H. Míguez, E. Chomski, F. García-Santamaría, M. Isabate, S. John, C. López, F. Meseguer, J. P. Mondía, G. A. Ozin, O. Toader, and H. M. Van Driel, Adv. Mater. (Weinheim, Ger.) **13**, 1634 (2001).
[25] A. Rugge, J. S. Becker, R. G. Gordon, and S. H. Tolbert, Nano Lett. **3**, 1293 (2003).
[26] V. F. Kozhevnikov, M. Diwekar, V. P. Kamaev, J. Shi, and Z. V. Vardeny, J. Phys.: Condens. Matter **338**, 159 (2003).
[27] T. B. Xu, Z. Y. Cheng, Q. M. Zhang, R. H. Baughman, C. Cui, A. A. Zakhidov, and J. Su, J. Appl. Phys. **88**, 405 (2000).
[28] V. N. Astratov, A. M. Adawi, M. S. Skolnick, V. K. Tikhomorov, V. Lyubin, D. G. Lidzey, M. Ariu, and A. L. Reynolds, Appl. Phys. Lett. **78**, 4094 (2001).
[29] J. S. King, C. W. Neff, C. J. Summers, W. Park, S. Blomquist, E. Forsythe, and D. Morton, Appl. Phys. Lett. **83**, 2566 (2003).
[30] A. Blanco, H. Míguez, F. Meseguer, C. López, F. López-Tejeira, and J. Sánchez-Dehesa, Appl. Phys. Lett. **78**, 3181 (2001).
[31] A. A. Zakhidov, R. H. Baughman, Z. Iqbal, C. X. Cui, I. Khayrullin, S. O. Dantas, I. Marti, and V. G. Ralchenko, Science **282**, 897 (1998).
[32] B. Li, J. Zhou, Q. Li, L. T. Li, and Z. L. Gui, J. Am. Ceram. Soc. **86**, 867 (2003).
[33] R. W. J. Scott, S. M. Yang, D. E. Williams, and G. A. Ozin, Chem. Commun. (Cambridge) **6**, 668 (2003).
[34] S. Gottardo, D. S. Wiersma, and W. L. Vos, J. Phys.: Condens. Matter **338**, 143 (2003).
[35] V. G. Solovyev, S. G. Romanov, C. M. S. Torres, M. Müller, R. Zentel, N. Gaponik, A. Eychmuller, and A. L. Rogach, J. Appl. Phys. **94**, 1205 (2003).
[36] M. Scharrer, X. Wu, A. Yamilov, H. Cao, and R. P. H. Chang, Appl. Phys. Lett. **86**, 151113 (2005).
[37] A. Blanco, E. Chomski, S. Grabtchak, M. Isabate, S. John, S. W. Leonard, C. López, F. Meseguer, H. Míguez, J. P. Mondía, G. A. Ozin, O. Toader, and H. van Driel, Nature (London) **405**, 437 (2000).
[38] F. García-Santamaría, M. Ibisate, I. Rodríguez, F. Meseguer, and C. López, Adv. Mater. (Weinheim, Ger.) **15**, 788 (2003).
[39] J. S. King, D. Heineman, E. Graugnard, and C. J. Summers, Appl. Surf. Sci. **244**, 511 (2005).
[40] J. S. King, E. Graugnard, and C. J. Summers, Adv. Mater. (Weinheim, Ger.) **17**, 1010 (2005).
[41] K. S. Yee, IEEE Trans. Antennas Propag. **AP-14**, 302 (1966).
[42] C. T. Chan, Q. L. Yu, and K. M. Ho, Phys. Rev. B **51**, 16635 (1995).
[43] H. Míguez, N. Tétreault, S. M. Yang, V. Kitaev, and G. A. Ozin, Adv. Mater. (Weinheim, Ger.) **15**, 597 (2003).
[44] M. Doosje, B. J. Hoenders, and J. Knoester, J. Opt. Soc. Am. B **17**, 600 (2000).